LOW ENERGY CONSUMPTION DESIGN METHOD AND STRATEGY FOR HIGH-ALTITUDE PROPELLERS BASED ON FLIGHT PROFILE

Miao Zhang[1,2,3,4], Jun Jiao[1], Jian Zhang[1], Zijian Zhang[1]

[1] Institute of Engineering Thermophysics, Chinese Academy of Sciences, Beijing 100190, China 1
[2] School of Aeronautics and Astronautics, University of Chinese Academy of Sciences, Beijing 100049, China 2
[3] National Key Laboratory of Science and Technology on Advanced Light-duty Gas-turbine, Beijing 100190, China 3
[4] Key Laboratory of UAV Emergency Rescue Technology, Ministry of Emergency Management, Beijing 102202, China 4

Abstract

The flight profile of solar-powered unmanned aerial vehicles (UAVs) typically includes various stages to achieve day-night energy cycling, which results in a large number of design points for the flight strategy. Therefore, it is necessary to conduct multi-point design optimization for high-altitude propellers to take full advantage of the motor power and reduce energy consumption. In the present study, the Co-Kriging model is used to conduct multi-point design optimization of high-altitude propellers to minimize the energy consumption of the propeller electric propulsion system throughout the entire flight profile. In addition, two design strategies for high-altitude propellers are presented. One strategy aims to maximize the combined efficiency of the propeller during climbing, high-altitude cruising, and low-altitude circling, and the other is to minimize the combined energy consumption of the propeller in these three stages. The results of these two design optimization strategies demonstrate a significant reduction in total energy consumption across the entire flight profile compared to the design optimization for a single design point. The strategy of minimizing the total energy consumption is more effective in reducing the overall energy consumption of the solar-powered UAVs throughout the entire flight profile, achieving a reduction of 10.39%.

Keywords: High-altitude propeller; Design optimization; Flight profile; Multi-point design; Co-Kriging.

1. Introduction

Solar-powered unmanned aerial vehicles (UAVs) rely on solar energy to stay in near space for days or longer [1]. However, constrained by the efficiency of battery packs and photovoltaic cells, solar-powered UAVs need to undergo various stages, including climbing, high-altitude cruising, descent, and low-altitude circling, to convert a portion of solar energy into gravitational potential energy, thereby enabling powered flight with day-night energy cycling. This flight strategy results in a larger range of design points for solar-powered UAVs [2, 3]. To maximize motor power utilization and minimize propeller energy consumption across the entire flight profile, it is necessary to conduct multi-point design optimization for high-altitude propellers.

In terms of design optimization of high-altitude propellers, D'Angelo S et al. [4] proposed a method for designing efficient propellers under given operating conditions. Danielle et al. [5] used the strip theory to design the high-altitude propeller for an aircraft cruising at 0.4 Mach (Ma) and an altitude of 25.9 km. Morgado et al. [6] developed the blade design software JBLADE based on the blade element momentum theory (BEMT) and incorporated a 3-D flow equilibrium condition to design the airship propeller. Park et al. [7] adopted the BEMT in conjunction with minimum induced loss and designed a solar-powered UAV propeller. Mourousias et al. [8] utilized various surrogate models and the vortex theory to optimize the propeller under a specific operating condition. However, these methods aim to ensure the propeller achieves maximum efficiency under specific operating conditions, which do not consider the attainment of overall maximum efficiency throughout the entire flight profile. Catana Razvan-Marius et.al [9] proposed a technical method that combined variable diameter and pitch to enhance the efficiency of propellers under different power modes. Wang et.al

[10] used the variation of pitch to maintain high efficiency over a wide range of rotational speeds for high-altitude propellers, thereby increasing the operational adaptability of these propellers. It is worth noting that adopting variable diameter and pitch can maintain high efficiency for high-altitude propellers even at off-design points, but this approach increases the weight of solar-powered UAVs and affects the overall reliability.

The objective of this work is to propose a strategy to minimize the energy consumption of the entire flight profile for the propeller electric propulsion system, along with a high-altitude propeller multi-point design method that considers both accuracy and efficiency. In this study, Co-Kriging surrogate model is used to conduct multi-point design optimization of high-altitude propellers to ensure that the energy consumption of high-altitude propellers is minimized throughout the flight profile. The high- and low-fidelity sample points are obtained using the optimal Latin hypercube sampling (OLHS) design method. The low-fidelity calculation method is based on blade element momentum theory (BEMT), while the high-fidelity calculation method relies on computational fluid dynamics (CFD) numerical simulation. Combining high- and low-fidelity calculation methods through a Co-Kriging surrogate model, using genetic algorithms (GA) to conduct multi-point optimization of the high-altitude propellers. Additionally, using the expected improvement (EI) infill-sampling criterion to judge the convergence of the objective function. Finally, the optimized results are subjected to CFD simulation analysis to assess the aerodynamic performance at various stages of the flight profile for solar-powered UAVs. In addition, two design strategies are presented, one aims to maximize the combined efficiency of the propeller during climbing, high-altitude cruising, and low-altitude circling, and the other aims to minimize the combined power consumption of the propeller in these three flight stages.

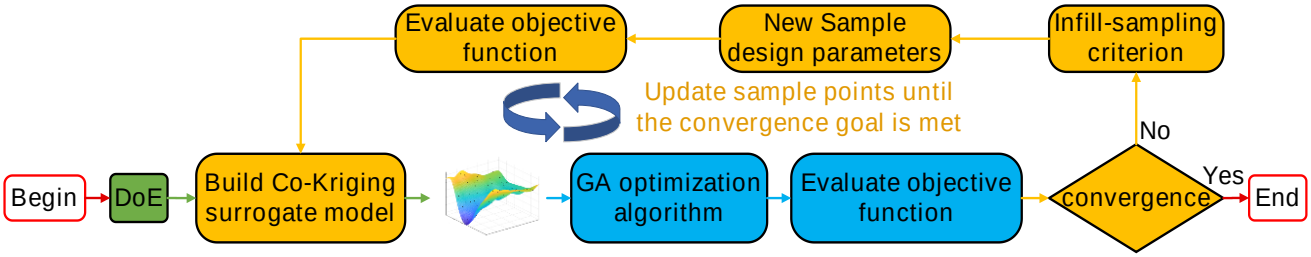

Figure 1 – Optimization process for high-altitude propeller.

2. METHOD

2.1 Blade element momentum theory

The BEMT uses radial discretization of the propeller blade into a finite number of sections. It accumulates the aerodynamic forces on each blade element along the radial direction to determine the overall aerodynamic force on the blade [11]. Figure 2 shows the principle of BEMT.

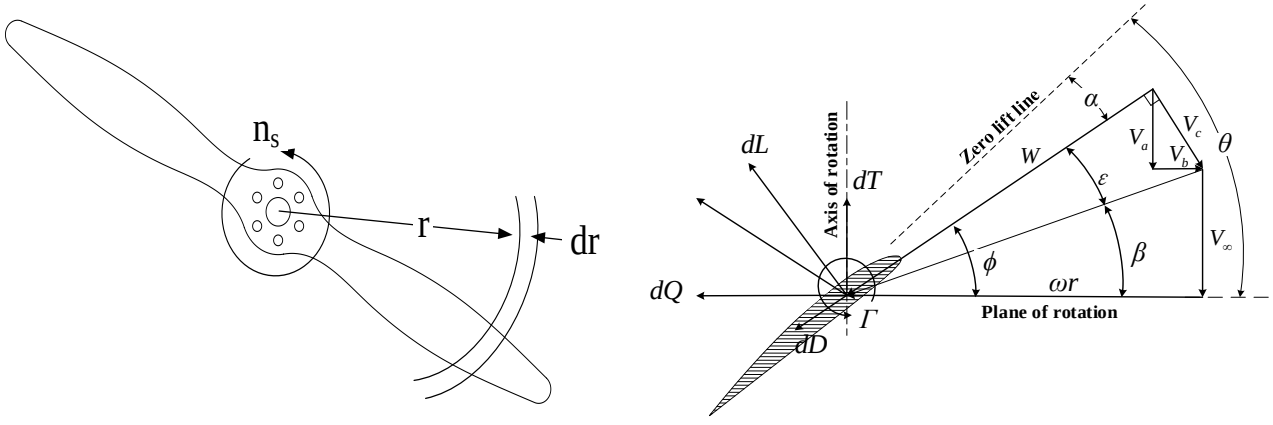

(a) – Front view of propeller (b) – Blade element at radius, r

Figure 2 – Section forces and velocities acting on a rotating propeller blade [12].

The radius of the blade element is r, the geometric blade pitch angle is θ, and the angle of the total

velocity W is Φ. The rotational speed and freestream velocity are ω, and V_∞; ε is the induced angle; V_c is the combined velocity of the axial and tangential induced velocities; and the axial and tangential induction factors are defined as a and b. Then the axial and tangential velocities of the blade element are $V_\infty + V_a$ and $\omega r - V_b$. The total velocity W relative to the blade is determined as

$$W = \sqrt{\left(V_\infty + aV_\infty\right)^2 + \left(\omega r - b\omega r\right)^2} \tag{1}$$

The angle of attack α of W relative to the blade element is given by

$$\alpha = \theta - \phi = \theta - \arctan\left(\frac{V_\infty + aV_\infty}{\omega r - b\omega r}\right) \tag{2}$$

Therefore, the thrust dT and torque dQ on a single blade element can be calculated by

$$dT = dL\cos\phi - dD\sin\phi = \frac{1}{2}\rho W^2 c\left(C_l\cos\phi - C_d\sin\phi\right)Bdr \tag{3}$$

$$dQ = r\left(dL\sin\phi + dD\cos\phi\right) = \frac{1}{2}\rho W^2 c\left(C_l\sin\phi + C_d\cos\phi\right)Brdr \tag{4}$$

Introducing the assumption of the propeller momentum theorem and the Bernoulli equation, the air in the plane of the propeller disk where the blade element dr is located satisfies the conservation of axial and radial momentum, leading to

$$dT = 4\pi\rho V_\infty^{\ 2} a\left(1+a\right)rFdr \tag{5}$$

$$dQ = 4\pi\rho V_\infty \omega b\left(1+a\right)r^3 Fdr \tag{6}$$

$$F = \frac{2}{\pi}\arccos\left\{\exp\left[\frac{B\left(R_p - r\right)}{2R_p\sin\phi}\right]\right\} \tag{7}$$

Where F is the Prandtl tip loss coefficient obtained considering the tip loss, and R_p is the propeller radius, B is the number of blades.

2.2 Computational fluid dynamics method

A multi-block structured grid is used to divide the spatial flow field around the propeller. The entire computational domain is divided into a stationary domain and a rotating domain. To simulate the rotation of the propeller, the Multiple Reference Frame (MRF) method is used, eliminating the need for transient calculations [13]. The rotational domain has a width of 1.5 times the diameter of the propeller and a length of 3 times the diameter of the propeller. The stationary domain has a width of 30 times the diameter of the propeller and a length of 60 times the diameter of the propeller. The inlet domain is defined with a speed far-field boundary condition, the outlet domain with a pressure far-field boundary condition, and the far domain with a pressure far-field boundary condition. The pressure and temperature values are set according to the real altitude. The blade surface is defined as a stationary, no-slip wall in relation to the adjacent zone. The number of propeller chordwise elements is 80, spanwise elements is 250, and the number of inflation layers is set to 50 layers.

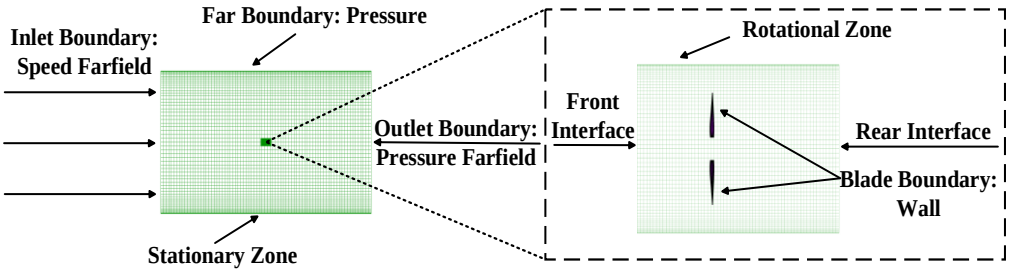

(a) – Representation of the calculation domain and its boundary conditions

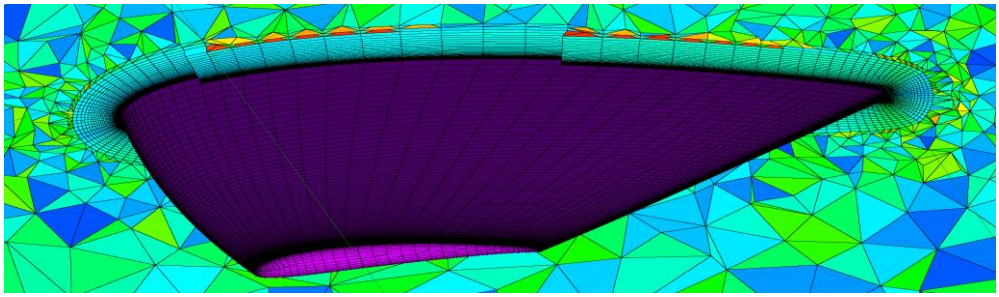

(b) – Distribution of the cells and boundary layer grid on the surface of the blade

Figure 3 – Meshing and boundary condition settings.

2.3 Co-Kriging surrogate model methods

The Co-Kriging fusion method is a self-regression model based on Bayesian theory, which can effectively consider the correlation among multiple credibility data. It utilizes cross-covariance to measure the correlation between different fidelity levels and integrates data of different accuracies. The purpose is to enhance predictive accuracy while achieving the best approximation of high-fidelity data across the expanse of the design space [14,15]. Furthermore, the Co-Kriging model inherits the inherent advantages of the Kriging model and can evaluate the uncertainty of the prediction points. While maintaining equivalent levels of approximate accuracy, it has the capacity to significantly enhance the efficiency of constructing a surrogate model [16].

The Co-Kriging model considers two sets of samples, $X_c = \{x_c^1,\ldots,x_c^{nc}\}$ and $X_e = \{x_e^1,\ldots,x_e^{ne}\}$, with dimension d obtained from the low-fidelity and high-fidelity simulator, respectively. The corresponding function values are represented by $y_c = \{y_c^1,\ldots,y_c^{nc}\}$ and $y_e = \{y_e^1,\ldots,y_e^{ne}\}$. The predicted values of the Co-Kriging model are defined as

$$\hat{y}_1(x) = \lambda^T y_s = \lambda_1^T y_c + \lambda_2^T y_e. \tag{8}$$

In the equation (8), λ_1 and λ_2 represent the weighted coefficients for the responses to high- and low-fidelity, respectively. Assuming the existence of two static stochastic processes corresponding to y_c and y_e,

$$\begin{cases} Y_c(x) = \beta_1 + Z_1(x) \\ Y_e(x) = \beta_2 + Z_2(x) \end{cases}. \tag{9}$$

The covariance and cross-covariance between random variables are defined as

$$\begin{cases} Cov\left(Z\left(x_1^{(i)}\right), Z\left(x_1^{(j)}\right)\right) = \sigma_1^2 R^{(11)}\left(x_1^{(i)}, x_1^{(j)}\right) \\ Cov\left(Z\left(x_2^{(i)}\right), Z\left(x_2^{(j)}\right)\right) = \sigma_2^2 R^{(22)}\left(x_2^{(i)}, x_2^{(j)}\right) \\ Cov\left(Z\left(x_1^{(i)}\right), Z\left(x_2^{(j)}\right)\right) = \sigma_1\sigma_2 R^{(12)}\left(x_1^{(i)}, x_2^{(j)}\right) \end{cases}. \tag{10}$$

In the equation (10), σ_1^2 and σ_2^2 represent the process variance of the stochastic processes $Y_1(x)$ and $Y_2(x)$, respectively. The estimated values of the Co-Kriging model are given by

$$\hat{y}_1(x) = \varphi^T \beta + r^T(x) R^{-1}\left(\tilde{y}_s - F\beta\right), \tag{11}$$

$$\begin{cases} \varphi = \begin{bmatrix} 1 \\ 0 \end{bmatrix} \\ \beta = \begin{bmatrix} \tilde{\beta}_1 \\ \tilde{\beta}_2 \end{bmatrix} = \left(F^T R^{-1} F \right)^{-1} F^T R^{-1} \tilde{y}_s \\ r = \begin{bmatrix} r_1(x) \\ r_2(x) \end{bmatrix} \\ \boldsymbol{R} = \begin{bmatrix} \boldsymbol{R}^{(11)} & \boldsymbol{R}^{(12)} \\ \boldsymbol{R}^{(21)} & \boldsymbol{R}^{(22)} \end{bmatrix} \\ \tilde{y}_s = \begin{bmatrix} y_c \\ \dfrac{\sigma_1}{\sigma_2} y_e \end{bmatrix} \\ F = \begin{bmatrix} 1 & 0 \\ 0 & 1 \end{bmatrix} \in \mathbb{R}^{\left(n_1 + n_2\right) \times 2} \end{cases}, \begin{cases} \boldsymbol{R}^{(11)} := \left(R^{(11)} \left(x_1^{(i)}, x_1^{(j)} \right) \right)_{i,j} \in \mathbb{R}^{n_1 \times n_1} \\ \boldsymbol{R}^{(12)} := \left(R^{(12)} \left(x_1^{(i)}, x_2^{(j)} \right) \right)_{i,j} = \left(\boldsymbol{R}^{(21)} \right)^T \in \mathbb{R}^{n_1 \times n_2} \\ \boldsymbol{R}^{(22)} := \left(R^{(22)} \left(x_2^{(i)}, x_2^{(j)} \right) \right)_{i,j} \in \mathbb{R}^{n_2 \times n_2} \\ r_1 := \left(R^{(11)} \left(x_1^{(i)}, x \right) \right)_i \in \mathbb{R}^{n_1} \\ r_2 := \left(R^{(12)} \left(x_2^{(i)}, x \right) \right)_i \in \mathbb{R}^{n_2} \end{cases} \tag{12}$$

3. High-altitude propeller design method and strategy

Figure 4 shows the flight profile during the task cycle of a solar-powered UAV. The solar-powered UAVs primarily contain four parts, including climbing, high-altitude cruising, descent, and low-altitude circling segments within a mission cycle. The descent stage primarily utilizes the potential energy difference resulting from changes in altitude to convert it into the energy required for the flight, therefore, it is not considered as a design point in the analysis. The single-point design is optimized with the goal of maximizing efficiency during the low-speed cruising stage of the solar-powered UAV. Considering the specific flight profile of a solar-powered UAV model, points A, B, and C are chosen as design points for multi-point design optimization. Throughout the entire design process, the weights of the three design points are allocated based on the proportion of the duration of each stage to the total duration of the three stages. In order to minimize the energy consumption of the entire flight profile for the propeller electric propulsion system, two design strategies are proposed for high-altitude propellers. One focuses on maximizing the overall efficiency of three points A, B, and C, while the other aims to minimize the total power consumption of the three points. Table – 1 shows the parameters of design points at each stage. The geometry of the blade is mainly determined by the distribution of chord and twist angle. To make the blade smooth and continuous, the cubic Bézier curve is used to describe the blade chord and the pitch angle distribution. This means that there are eight design variables, c_1, c_2, c_3, c_4, β_1, β_2, β_3, β_4. The rotation speed, n_s, varies throughout the design process, and thus, n_s is considered as the ninth design variable. The required thrust, T_{min}, under the flight condition and the rated power, P_{rated}, absorbed from the motor are both restricted based on the task requirement and energy system. The aerodynamic optimization problem for the two high-altitude propeller design optimization strategies is presented through equation (17) and equation (18).

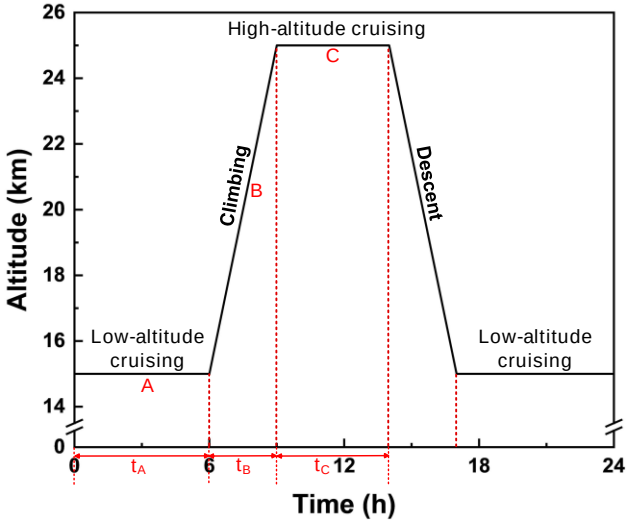

Figure 4 – Flight profile during the task cycle.

Table – 1 Different design point parameters.

Stage	flight speed / ($m \cdot s^{-1}$)	Design thrust / (N)	Air density / ($kg \cdot m^{-3}$)	Dynamic viscosity / [$kg(m \cdot s)^{-1}$]	Weighted values
A – Climbing	33	100	0.08891	$1.42161*10^{-5}$	0.143
B – High-altitude cruising	45	50	0.04008	$1.44842*10^{-5}$	0.238
C – low-altitude circling	24	42	0.19476	$1.42161*10^{-5}$	0.619

$$\begin{aligned} &\text{maximize} \quad w_A \cdot \eta_A + w_B \cdot \eta_B + w_C \cdot \eta_C \\ &\text{design variables} \quad c_1, c_2, c_3, c_4, \beta_1, \beta_2, \beta_3, \beta_4, n_s \\ &\text{subject to} \quad \begin{cases} T \geq T\min \\ P_{shaft} \leq P_{rated} \\ Ma_{tip} \leq Ma_{\max} \end{cases} \end{aligned} \tag{13}$$

$$\begin{aligned} &\text{minimize} \quad t_A \cdot P_A + t_B \cdot P_B + t_C \cdot P_C \\ &\text{design variables} \quad c_1, c_2, c_3, c_4, \beta_1, \beta_2, \beta_3, \beta_4, n_s \\ &\text{subject to} \quad \begin{cases} T \geq T\min \\ P_{shaft} \leq P_{rated} \\ Ma_{tip} \leq Ma_{\max} \end{cases} \end{aligned} \tag{14}$$

The propeller has two blades, utilizing the Eppler 387 airfoil, and the diameter of the propeller is 2.5 meters. Each design point employs 1000 low-fidelity sample points and 200 high-fidelity sample points to construct the surrogate model. Figure 5 presents the design optimization results based on maximizing the overall efficiency, while Figure 6 shows the design optimization results based on minimizing the total power consumption.

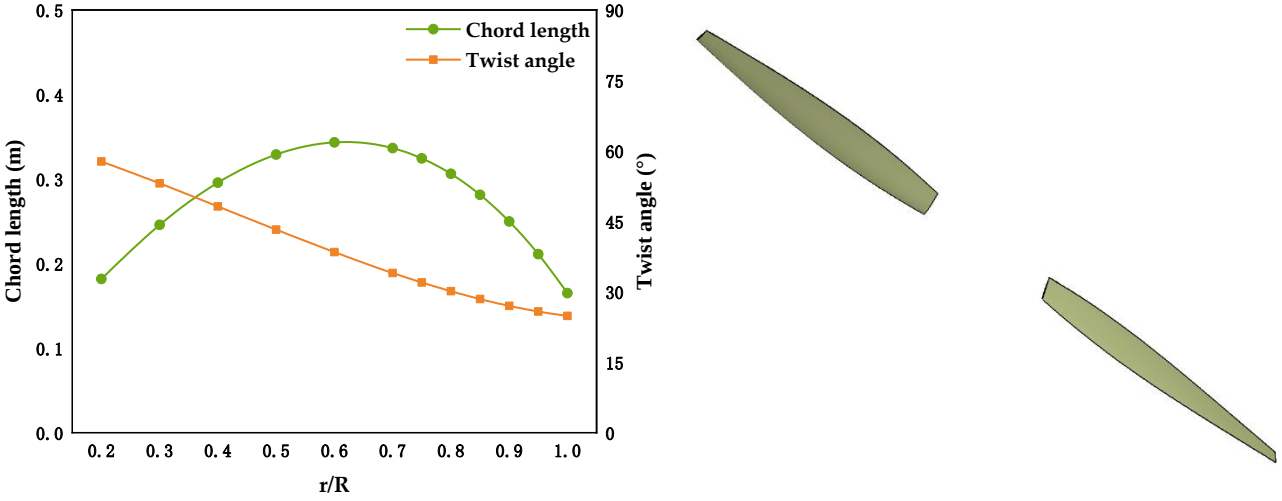

(a) Chord and pitch angle distribution. (b) Propeller model.

Figure 5 – The design optimization results based on maximizing the overall efficiency.

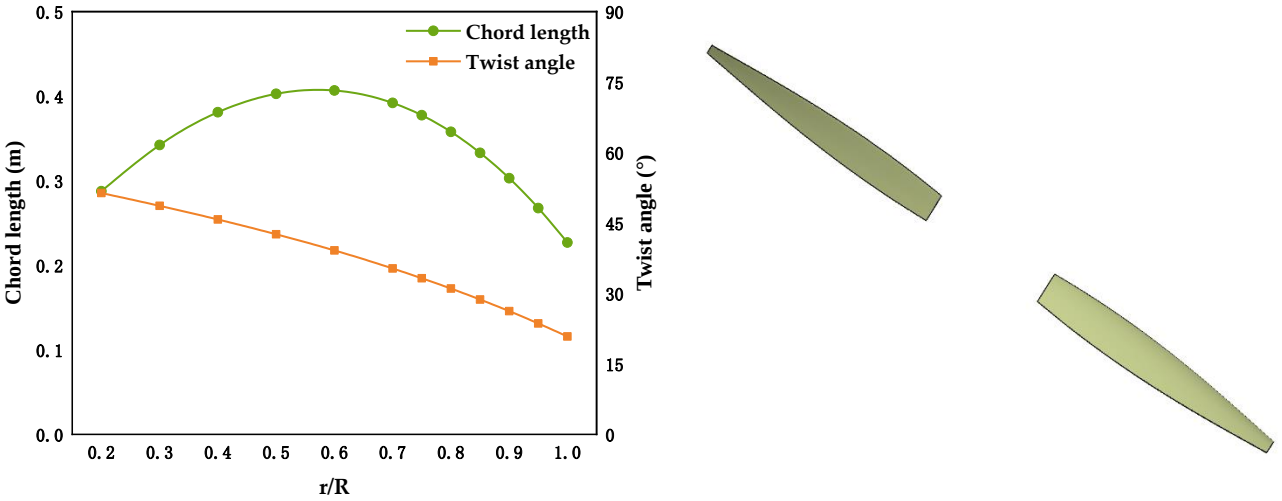

(a) Chord and pitch angle distribution. (b) Propeller model.

Figure 6 – The design optimization results based on minimizing the total power consumption.

The CFD method is used to perform numerical simulations on the two design optimization results, and the energy consumption of the two high-altitude propellers throughout the entire flight profile is calculated. The results are shown in Figure 7.

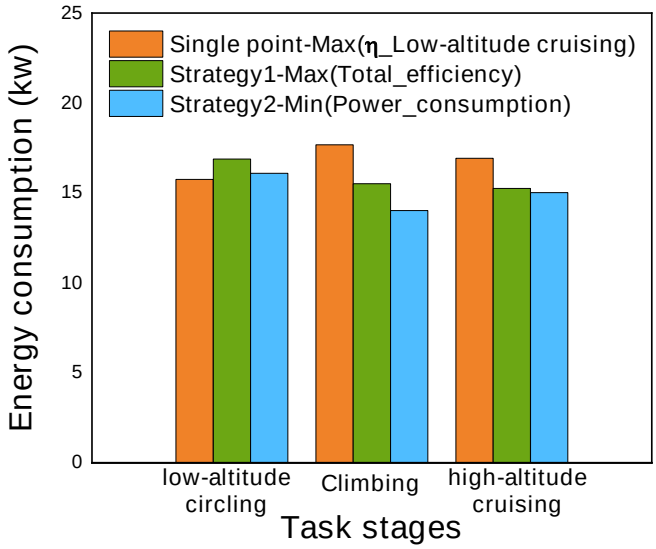

Figure 7 –Energy consumption across different task stages.

As shown in Figure 7, Although the single-point design consumes less energy at the design point, considering the entire flight profile, the total energy consumption of the multi-point design is lower than that of the single-point design. Compared to the single-point design results, strategy 1 reduces energy consumption by 5.38% over one flight cycle, while strategy 2 reduces energy consumption by 10.39%. Regarding the multi-point design, Under the premise of meeting the thrust requirements of the solar-powered UAV at various flight stages, the design strategy 2 is more advantageous. Compared to the design strategy 1, the strategy 2 demonstrates lower energy usage across all stages of the flight profile. Notably, during the climb phase, the high-altitude propeller designed with strategy 2 exhibits a significant advantage, consuming 9.62% less energy than strategy 1. Over the entire flight cycle, strategy 2 achieves an 5.290% reduction in energy consumption. Overall, for solar-powered UAVs, the design strategy based on minimizing flight profile energy consumption can save more energy.

4. Conclusions and discussions

The Co-Kriging surrogate model is used to perform multi-point design optimization of high-altitude propellers. Two design optimization strategies are proposed based on the flight profiles of solar-powered drones. One goal is to maximize the overall efficiency of the high-altitude propeller, and the other goal is to minimize the total energy consumption of the high-altitude propeller. The CFD numerical simulation method is used to compare the aerodynamic performance across various mission stages for solar-powered UAVs and the total energy consumption of the flight profile between the multi-point design results and the single-point design results. Compared to the single-point design results, the strategy of maximizing overall efficiency reduces energy consumption by 5.38% over one flight cycle, while the strategy of minimizing total energy consumption reduces energy consumption by 10.39%. Furthermore, when comparing the two high-altitude propeller design optimization strategies proposed in this paper, the strategy focused on minimizing the total energy consumption throughout the flight profile is more effective in reducing the overall energy consumption of the solar-powered UAVs, achieving an additional 5.29% reduction in energy consumption.

5. Contact Author Email Address

Miao Zhang: zhangmiao@iet.cn

6. Copyright Statement

The authors confirm that they, and/or their company or organization, hold copyright on all of the original material included in this paper. The authors also confirm that they have obtained permission, from the copyright holder of any third party material included in this paper, to publish it as part of their paper. The authors confirm that they give permission, or have obtained permission from the copyright holder of this paper, for the publication and distribution of this paper as part of the ICAS proceedings or as individual off-prints from the proceedings.

References

[1] Ni Wenjun, Bi Ying, Wu Di, et al. Energy-optimal trajectory planning for solar-powered aircraft using soft actor-critic[J]. *Chinese Journal of Aeronautics*, 2022, 35(10): 337-353.

[2] Rajendran P, Smith H. Implications of longitude and latitude on the size of solar-powered UAV[J]. *Energy conversion and management*, 2015, 98: 107-114.

[3] Cestino E. Design of solar high-altitude long endurance aircraft for multi payload & operations[J]. *Aerospace science and technology*, 2006, 10(6): 541-550.

[4] D'Angelo S, Berardi F, Minisci E. Aerodynamic performances of propellers with parametric considerations on the optimal design[J]. *The Aeronautical Journal*, 2002, 106(1060): 313-320.

[5] Koch L D. Design and performance calculations of a propeller for very high-altitude flight[R]. 1998.

[6] Morgado J, Silvestre M Â R, Páscoa J C. Validation of new formulations for propeller analysis[J]. *Journal of Propulsion and Power*, 2015, 31(1): 467-477.

[7] Park D, Lee Y, Cho T, et al. Design and performance evaluation of propeller for solar-powered high-altitude long-endurance unmanned aerial vehicle[J]. *International Journal of Aerospace Engineering*, 2018, 2018.

[8] Mourousias N, Malim A, Marinus B G, et al. Assessment of multi-fidelity surrogate models for high-altitude propeller optimization[C]//*AIAA AVIATION 2022 Forum*. 2022: 3752.

[9] Catana R, Cican G. Global Study of the Performance of a Propeller with a Variable Pitch and a Variable Diameter[J]. *Applied Mechanics and Materials*, 2016, 841: 298-302.

[10] Dongchen W, Bifeng S, Jun J, et al. High-altitude airship variable-pitch propeller performance analysis at multiple altitudes[J]. *Proceedings of the Institution of Mechanical Engineers, Part G: Journal of Aerospace Engineering*, 2023: 09544100231167710.

[11] Mourousias N, García-Gutiérrez A, Malim A, et al. Uncertainty quantification study of the aerodynamic performance of high-altitude propellers[J]. *Aerospace Science and Technology*, 2023, 133: 108108.

[12] Jiao J, Song B F, Zhang Y G, et al. Optimal design and experiment of propellers for high-altitude airship[J]. *Proceedings of the Institution of Mechanical Engineers, Part G: Journal of Aerospace Engineering*, 2018, 232(10): 1887-1902.

[13] Morgado J, Abdollahzadeh M, Silvestre M A R, et al. High-altitude propeller design and analysis[J]. *Aerospace Science and Technology*, 2015, 45: 398-407.

[14] Forrester A I J, Sóbester A, Keane A J. Multi-fidelity optimization via surrogate modelling[J]. *Proceedings of the royal society a: mathematical, physical and engineering sciences*, 2007, 463(2088): 3251-3269.

[15] Couckuyt I, Forrester A, Gorissen D, et al. Blind Kriging: Implementation and performance analysis[J]. *Advances in Engineering Software*, 2012, 49: 1-13.

[16] Liu X, Wan D, Lei L. Multi-fidelity model and reduced-order method for comprehensive hydrodynamic performance optimization and prediction of JBC ship[J]. *Ocean Engineering*, 2023, 267: 113321.